



# The Host Galaxies of Hybrid Morphology Radio Sources

Andra Stroe<sup>1,6</sup> , Victoria Catlett<sup>1,2</sup> , Jeremy J. Harwood<sup>3</sup> , Tessa Vernstrom<sup>4</sup> , and Beatriz Mingo<sup>5</sup> <sup>1</sup>Center for Astrophysics | Harvard & Smithsonian, 60 Garden Street, Cambridge, MA 02138, USA; [andra.stroe@cfa.harvard.edu](mailto:andra.stroe@cfa.harvard.edu)<sup>2</sup>The University of Texas at Dallas, 800 W Campbell Rd, Richardson, TX 75080, USA<sup>3</sup>Centre for Astrophysics Research, School of Physics, Astronomy and Mathematics, University of Hertfordshire, College Lane, Hatfield, Hertfordshire AL10 9AB, UK<sup>4</sup>ICRAR, The University of Western Australia, 35 Stirling Highway, 6009 Crawley, Australia<sup>5</sup>School of Physical Sciences, The Open University, Walton Hall, Milton Keynes, MK7 6AA, UK

Received 2022 August 12; revised 2022 October 13; accepted 2022 October 14; published 2022 December 16

## Abstract

Based on their differing radio morphologies, powerful radio galaxies can be separated into the Fanaroff–Riley I (FR I) and II (FR II) classes. Hybrid morphology radio sources (HyMoRS) contain morphologies consistent with each type of jet on either side: a powerful, highly relativistic FR I–like jet terminating in a hotspot on one side and an FR I–like plume on the other. HyMoRS present a unique opportunity to study the conditions that give rise to the dichotomy. Using host galaxy properties, we conduct the first multiwavelength investigation into whether orientation can explain HyMoRS morphology. Through optical spectroscopy and mid-infrared photometry, we analyze the emission characteristics, and evaluate the broad characteristics of five HyMoRS host galaxies at intermediate redshifts ( $0.4 < z < 1.5$ ). The HyMoRS host galaxies in our sample have properties consistent with typical host galaxies of FR II sources, suggesting that the observed hybrid morphologies may be caused by a dense, cluster-like environment bending FR II jets combined with a favorable orientation that can make one side appear similar to an FR I jet. Our results thus support the hypothesis that HyMoRS are mainly caused by environment and orientation.

*Unified Astronomy Thesaurus concepts:* [Active galaxies \(17\)](#); [Early-type galaxies \(429\)](#); [Emission line galaxies \(459\)](#); [Fanaroff–Riley radio galaxies \(526\)](#); [Galaxy clusters \(584\)](#); [Galaxy environments \(2029\)](#); [Galaxy evolution \(594\)](#); [Ionization \(2068\)](#); [Radio galaxies \(1343\)](#); [Spectroscopy \(1558\)](#)

## 1. Introduction

The prominent radio emission in powerful active galactic nuclei (AGN) typically manifests through twin, symmetrical relativistic jets, spanning several hundreds of kiloparsec to megaparsec scales outward from their host galaxy. Fanaroff & Riley (1974) divided powerful radio sources into two morphological classifications, Fanaroff–Riley class I (FR I) and class II (FR II). In FR I sources, the emission is brightest near the host galaxy, followed by extended diffuse emission outwards. On the other hand, FR IIs feature prominent brightness peaks called “hotspots” farther from the host galaxy with lobes of diffuse emission. The different morphology was later attributed to differing jet physics: unlike FR I jets, which get disrupted quickly within the host and decelerate on tens of kiloparsec scales, FR II jets stay collimated over large distances (Bicknell 1994; Laing & Bridle 2002).

The underlying cause of the FR I/II dichotomy has been a topic of debate (e.g., Kaiser & Alexander 1997), and theories include both intrinsic and extrinsic causes. For example, the properties of the black hole engine could affect the magnetic fields that collimate and power the jets (e.g., Celotti et al. 1997), which could determine the initial jet velocities. The material in the host galaxy could affect the deceleration of the jet material (e.g., Kaiser & Best 2007; Mingo et al. 2019). This

scenario is supported by the observed differences between the host galaxies of FR I and FR II sources (e.g., Miraghaei & Best 2017). FR I sources are hosted by massive red elliptical galaxies with spectra dominated by absorption features, no broad lines, and little-to-no narrow emission lines (e.g., Matthews et al. 1964; Hickox et al. 2009; Best & Heckman 2012; Janssen et al. 2012; Butler et al. 2018). At low jet power, both FR Is and FR IIs are predominantly low-excitation radio galaxies (LERGs; Laing et al. 1994; Mingo et al. 2022). High-excitation radio galaxies (HERG) appear at high jet powers, in which FR IIs dominate. HERGs, hosted by bluer galaxies with lower masses, higher star formation rates (SFR), and diskier morphologies, have strong narrow (an order of magnitude stronger than LERGs) and, in some cases broad, emission lines (e.g., Baum & Heckman 1989; Zirbel & Baum 1995; Best & Heckman 2012; Miraghaei & Best 2017; Butler et al. 2018). Finally, FR Is tend to live in denser cluster environments than FR II galaxies, suggesting that the density of the intergalactic/intracluster medium could decelerate the jets outside of the galaxy (e.g., Prestage & Peacock 1988; Mingo et al. 2019).

Hybrid morphology radio sources (HyMoRS) possess both FR I and FR II structures, presenting a unique opportunity to probe the conditions that cause the dichotomy. First identified in Gopal-Krishna & Wiita (2000), their existence suggests that the black hole engine cannot alone cause the morphological differences between FR Is and FR IIs. The number of HyMoRS candidates has rapidly grown over the past few years, amounting to hundreds of sources and  $\sim 5\%$  of the resolved radio AGN population in modern radio surveys (Mingo et al. 2019; Kapińska et al. 2017).

<sup>6</sup> Clay Fellow.



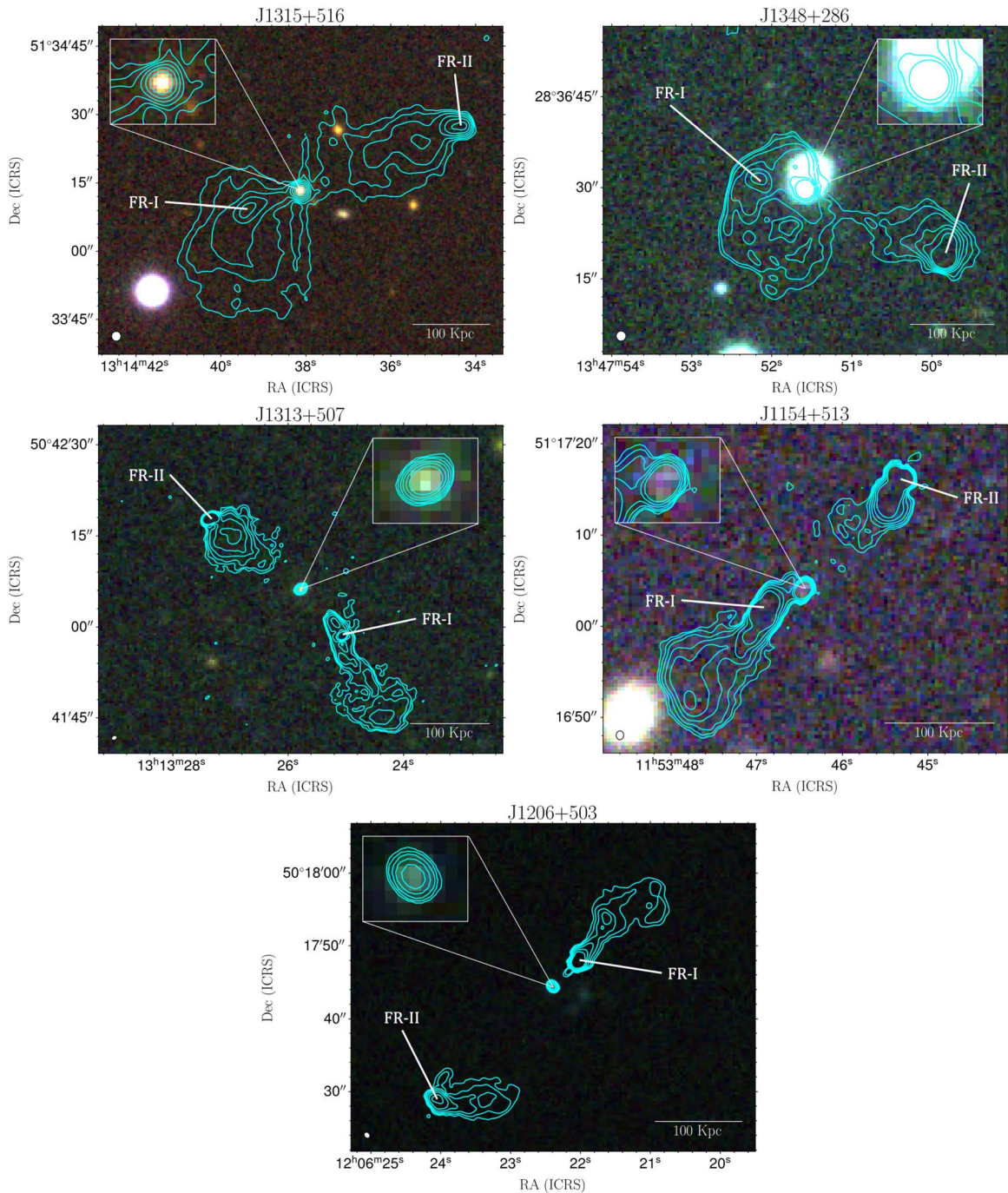


**Figure 1.** The five HyMoRS in our sample. The background images are Pan-STARRS RGB composites (using  $g$ ,  $r$ ,  $i$  filters), with overlaid  $L$ -band VLA contours at  $\sigma_{\text{rms}} \times 2''$ . Each image shows the host galaxy (zoomed-in section) with an FR I-like plume on one side and an FR II jet, hotspot, and lobe on the other.

In this paper, using the intrinsic properties of the host galaxy, we investigate whether orientation can give rise to these morphological differences. As a relativistic jet from the black hole engine travels through the host galaxy, it may be slowed down by intervening material in a host galaxy or travel unimpeded and slow down on larger scales, eventually terminating in a bright hotspot (e.g., Kaiser & Best 2007; Mingo et al. 2019). The distribution and type of material in the galaxy could affect how quickly the jet slows, affecting the location of the final emission peak (Gopal-Krishna & Wiita 1996). We aim to unveil the cause of the dichotomy by focusing our analysis on the best-studied five sources that

Gawroński et al. (2006) securely identified as HyMoRS given their spatially resolved radio observations (see Figure 1 and Table 1).  $L$ -band (1.0–2.0 GHz) images from the Very Large Array (VLA) show the presence of one FR I-like and one FR II set of structures in each system, but, using spectral aging techniques, Harwood et al. (2020) largely attribute the FR I-like morphology to a favorable projection of an FR II jet, hotspot, and lobe. We measure detailed galaxy properties by investigating their spectral properties with newly obtained 1D spectroscopy from the Gemini Multi-Object Spectrograph-North (GMOS-N) in combination with mid-IR color diagnostics.

**Table 1**

Positions, Spectroscopic Redshifts ( $z_{\text{spec}}$ ), Spectrum Origin Instrument, SDSS Magnitudes in the  $g$ ,  $r$ , and  $i$  Bands, and Radio Fluxes (at 1.4 GHz and 4.9 GHz) for Each of the Five HyMoRS in Our Sample

Source	R.A. (hh mm ss)	Decl. ( $^{\circ}$ $'$ $''$ )	$z_{\text{spec}}$	Instrument	$g$ (mag)	$r$ (mag)	$i$ (mag)	$S_{1.4\text{ GHz}}$ (mJy)	$S_{4.9\text{ GHz}}$ (mJy)
J1315+516	13 14 38.12	51 34 13.4	0.47799	SDSS	$20.52 \pm 0.03$	$19.75 \pm 0.02$	$18.98 \pm 0.02$	93	51
J1348+286	13 47 51.58	28 36 29.6	0.74058	BOSS	$17.39 \pm 0.01$	$17.20 \pm 0.01$	$17.43 \pm 0.01$	241	117
J1313+507	13 13 25.78	50 42 06.2	0.88000	GMOS	$21.45 \pm 0.05$	$20.96 \pm 0.05$	$20.36 \pm 0.04$	277	84
J1154+513	11 53 46.43	51 17 04.1	1.37250	GMOS	$22.10 \pm 0.12$	$21.44 \pm 0.11$	$21.37 \pm 0.16$	495	137
J1206+503	12 06 22.39	50 17 44.3	1.45423	BOSS	$21.38 \pm 0.04$	$20.89 \pm 0.04$	$20.69 \pm 0.05$	241	75

In Section 2, we present our new data taken with Gemini, as well as archival images and spectra, and we walk through the data reduction methods. Section 3 discusses how we analyze the spectral and ancillary data. In Section 4, we discuss the insights into HyMoRS host galaxy properties and the implications for the broader formation context of powerful radio galaxies. Conclusions can be found in Section 5.

We use the  $\Lambda$ CDM cosmological model of a flat universe with  $H_0 = 71 \text{ km s}^{-1} \text{ Mpc}^{-1}$ ,  $\Omega_m = 0.27$ , and  $\Omega_\Delta = 0.73$ . A Salpeter (1955) initial mass function is used throughout.

## 2. Sample, Observations, and Data Reduction

### 2.1. HyMoRS Sample

The five sources in this study have been identified as bona fide HyMoRS through a uniform radio selection by Gawroński et al. (2006). After selecting all sources with 1.4 GHz fluxes  $>20$  mJy and angular size  $\theta > 8''$  in five random high galactic latitude  $\approx 16^\circ \times 16^\circ$  areas within the VLA Faint Images of the Radio Sky at Twenty-Centimeters survey (White et al. 1997), Gawroński et al. (2006) visually selected HyMoRS candidates and followed them with pointed, narrow-band VLA observations, resulting in a secure sample of five HyMoRS. The resolved spatial and spectral radio properties of these five sources were then studied in detail by Harwood et al. (2020) through high-resolution, wide-band (C, L), JVLA observations. In the present paper, we follow up these five best-studied sources, without imposing any additional selection criteria.

### 2.2. GMOS-N Observations and Data Reduction

The optical spectra from the GMOS-N long-slit instrument are new to this paper (PI: Stroe). We observed the three sources without existing spectroscopic observations: J1313+507, J1154+513, and J1206+503, with GMOS-N in long-slit mode. To obtain a continuous wavelength coverage between 5000 and 10000 Å, we used the R150 grating centered at 8000 and 8500 Å, in combination with the GG455 filter, a 1Prime slit and  $2 \times 2$  binning, resulting in 23 Å resolution. The data were collected in 2019 March, taking advantage of the poorer observing conditions on Maunakea, with  $\geq 70$ –100 percentile cloud coverage, and  $\geq 70$ – $\geq 85$  percentile overall image quality. J1313+507 and J1206+503 were observed over four exposures, for a total time on target of 44 minutes. J1154+513 was observed for 55 minutes, to compensate for the very poor cloud coverage during the last exposure. We also observed the standard star Hiltner 600 for flux calibration. Note that, subsequently, a higher quality Baryon Oscillation Spectroscopic Survey (BOSS) spectrum for J1206+503 was made public (described below), which was used in the rest of the paper.

We reduced the GMOS-N spectra from the Gemini North telescope for J1313+507 and J1154+513 according to the GMOS Data Reduction Cookbook using the Gemini IRAF package (Shaw 2016). First, all exposures were debiased, and we flat fielded the science frames and the standard star exposure. Next, we derived a wavelength solution for each instrumental setup by manually identifying emission lines in the arc spectra, resulting in a typical rms of 5–8 Å. Next, we removed cosmic rays from the science exposures using Laplacian Cosmic Ray Identification (LACOS) from van Dokkum (2001). We then subtracted the sky in each exposure by using emission-free sky areas adjacent to the target trace. We extracted a 1D spectrum from each exposure using a 14'' area and median combined all four exposures for each target to improve the signal-to-noise ratio (S/N). Finally, we applied the sensitivity solution derived from an exposure of the standard star Hiltner 600, creating the final GMOS-N spectrum. The resulting spectra can be found in Figure 2.

### 2.3. Ancillary Data

Spectroscopy for J1206+503, J1315+516, and J1348+286 was extracted from the Sloan Digital Sky Survey (SDSS) DR16 archives (Ahumada et al. 2020) and used either the SDSS or the BOSS spectrograph (Dawson et al. 2013). The SDSS/BOSS data cover the  $\sim 4000$ –9000 Å range, at a resolution of 3.6 Å.

To supplement the optical spectroscopy, we compiled optical and mid-IR photometry for all the sources using the VizieR catalog (Ochsenbein et al. 2000), including data from the Panoramic Survey Telescope and Rapid Response System (Pan-STARRS; Flewelling et al. 2020), and the Wide-field Infrared Survey Explorer (WISE; Wright et al. 2010, 2019).

## 3. Analysis

We created red–green–blue (RGB) composite images with radio contours using  $g$ ,  $r$ ,  $i$  Pan-STARRS (Flewelling et al. 2020) and  $L$ -band VLA images (Harwood et al. 2020). The optical data enabled a clear identification of the host galaxy, while the FR-I -like jet and plume and the FR II jet, hotspot, and lobe were easily distinguished in the radio images.

### 3.1. Spectral Lines

To probe SF and AGN activity within the sources, we identified prominent rest-frame optical and UV emission lines in each source using the Galaxy Line Emission & Absorption Modeling (GLEAM) software (Stroe & Savu 2021). For each potential emission line, GLEAM searches for emission peaks near the expected central wavelength, omitting two ranges that feature prominent telluric absorption in our analysis (7586–7658 Å 6864–6945 Å). Once it identifies an emission line and its adjacent

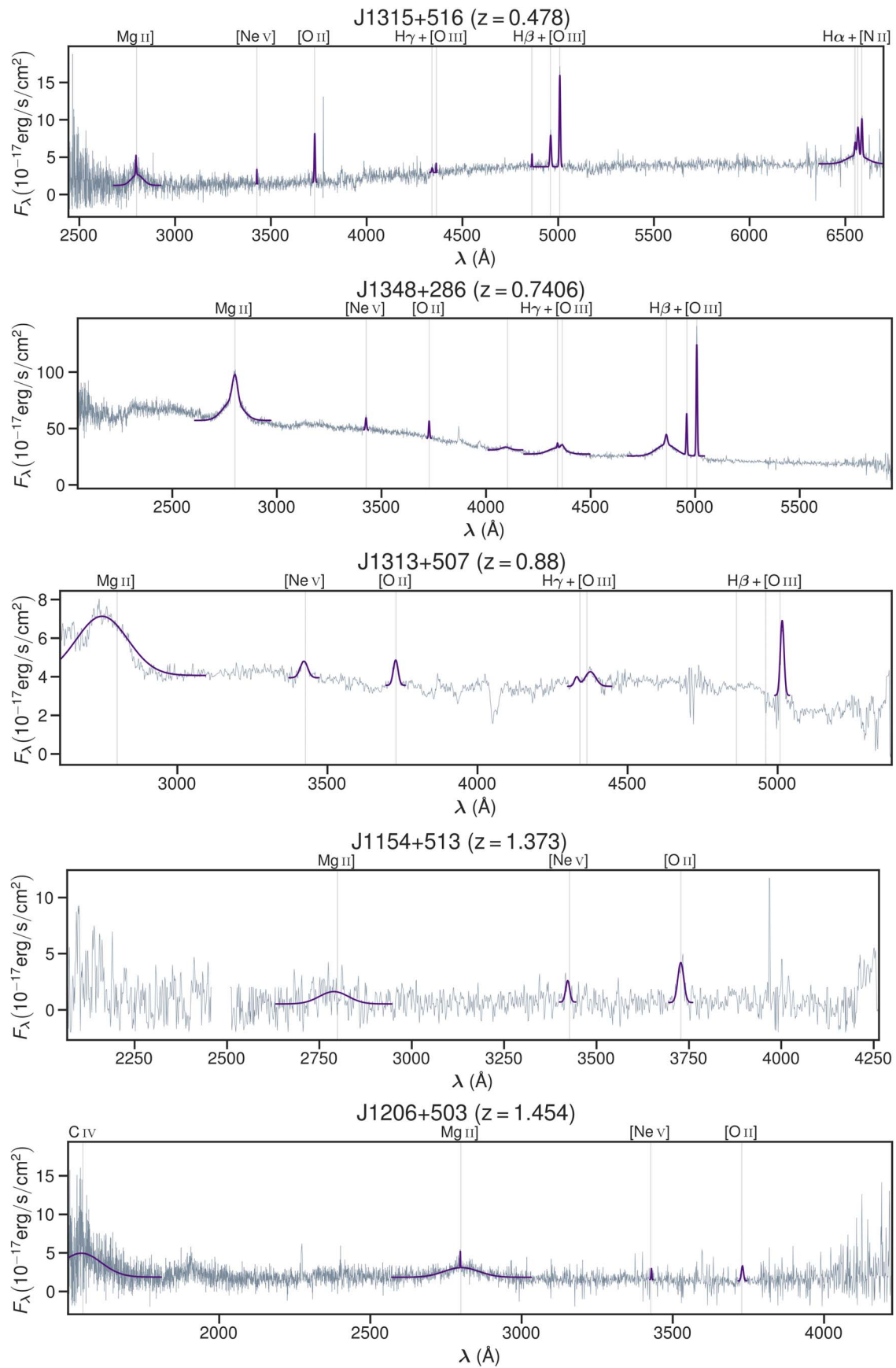


**Figure 2.** HyMoRS spectra with a selection of emission lines marked (gray vertical lines). Gaussian emission line fits are overplotted in the purple lines. All of our sources have prominent narrow and broad emission lines typical of Type 2 AGN and quasars, with [O II] emission suggesting significant SFRs. The line luminosities and velocity FWHMs are listed in Tables 2 and 3, respectively.

**Table 2**  
Luminosities for Select UV and Optical Emission Lines

Line	$\lambda_{\text{vac}}$ (Å)	J1315+516 ( $10^{40}$ erg s $^{-1}$ )	J1348+286 ( $10^{40}$ erg s $^{-1}$ )	J1313+507 ( $10^{40}$ erg s $^{-1}$ )	J1154+513 ( $10^{40}$ erg s $^{-1}$ )	J1206+503 ( $10^{40}$ erg s $^{-1}$ )
C IV	1549.48					6876 ± 1326
C III] (narrow)	1908.734					70 ± 23
C III] (broad)	1908.734					1276 ± 148
C II] (narrow)	2326.0		<25		<309	<19
C II] (broad)	2326.0		821 ± 138		<309	238 ± 72
Mg II (narrow)	2799.12	12 ± 3	1816 ± 146	<17	<83	44 ± 21
Mg II (broad)	2799.12	93 ± 12	5032 ± 183	2533 ± 108	1252 ± 279	2445 ± 219
[Ne V]	3426.85	4 ± 2	198 ± 24	102 ± 15	305 ± 54	60 ± 21
[O II]	3728.483	36 ± 2	234 ± 36	100 ± 10	827 ± 61	228 ± 29
[Ne III]	3868.76	10 ± 3	261 ± 44	26 ± 9	<104	<43
H $\delta$	4102.89	<2	316 ± 80	<14		<102
H $\gamma$ (narrow)	4341.68	4 ± 2	62 ± 17	33 ± 15		
H $\gamma$ (broad)	4341.68	<1	1321 ± 94	<14		
H $\beta$ (narrow)	4862.68	5 ± 1	310 ± 36	<23		
H $\beta$ (broad)	4862.68	<1	2884 ± 100	<23		
[O III]	4960.295	33 ± 2	610 ± 73	<24		
[O III]	5008.24	81 ± 3	1729 ± 100	229 ± 21		
[N II]	6549.86	11 ± 4				
H $\alpha$ (narrow)	6564.614	33 ± 5				
H $\alpha$ (broad)	6564.614	124 ± 18				
[N II]	6585.27	35 ± 4				

**Note.** Adjacent lines were fit together, and both narrow and broad components were fit where necessary.

**Table 3**  
Deconvolved Emission Line Velocity Widths

Line	$\lambda_{\text{vac}}$ (Å)	J1315+516 (km s $^{-1}$ )	J1348+286 (km s $^{-1}$ )	J1313+507 (km s $^{-1}$ )	J1154+513 (km s $^{-1}$ )	J1206+503
C IV	1549.48					30066 ± 4698
C III] (narrow)	1908.734					336 ± 138
C III] (broad)	1908.734					12805 ± 1469
C II]	2326.0		8648 ± 1429			4358 ± 1401
Mg II (narrow)	2799.12	460 ± 140	3126 ± 174			
Mg II (broad)	2799.12	7736 ± 1003	11457 ± 445	21664 ± 748	9836 ± 2051	14533 ± 1051
[Ne V]	3426.85	95 ± 59	579 ± 81	2332 ± 393	754 ± 225	230 ± 87
[O II]	3728.483	455 ± 27	456 ± 81	1148 ± 166	1299 ± 124	654 ± 99
[Ne III]	3868.76	525 ± 123	656 ± 128			
H $\delta$	4102.89		3569 ± 936	9589 ± 2102		
H $\gamma$ (narrow)	4341.68	448 ± 257	344 ± 98	860 ± 555		
H $\gamma$ (broad)	4341.68		6403 ± 375			
[O III]	4364.436		1402.0 ± 288.0	2730 ± 573		
H $\beta$ (narrow)	4862.68	158 ± 42	795 ± 83			
H $\beta$ (broad)	4862.68		6641 ± 241			
[O III]	4960.295	508 ± 35	362 ± 49			
[O III]	5008.24	413 ± 13	378 ± 22	468 ± 88		
H $\alpha$ (narrow)	6564.614	430 ± 61				
H $\alpha$ (broad)	6564.614	5347 ± 773				
[N II]	6585.27	337 ± 37				

continuum, GLEAM fits a Gaussian profile to the emission to derive parameters, such as the total flux and equivalent width. Lines located nearby are jointly fit, and C III], C II], Mg II, H $\gamma$ , H $\beta$ , and H $\alpha$  were fit with a two-component Gaussian, as required to identify any broad and narrow components. A line was considered a detection when  $S/N > 3$ . For undetected lines, we calculated  $3\sigma$  upper flux limits. The luminosities of the fitted lines are listed in Table 2. For resolved lines, we also calculate the velocity FWHM  $v_{\text{FWMH}}$  (see Table 3).

As well as the velocity width of the lines, the narrow-line components of the [N II]/H $\alpha$  and [O III]/H $\beta$  ratios can be used

to distinguish between star-forming galaxies and AGN (see Figure 3; Baldwin et al. 1981, Baldwin–Phillips–Terlevich (BPT) diagram). We included sample galaxy data from SDSS DR7 on this diagram for comparison (Abazajian et al. 2009).

### 3.2. Star Formation Rates

H $\alpha$  cannot reliably be used to estimate the SFR of the host galaxy when an AGN is present. However, we can use [O II] luminosities to roughly estimate SFRs, since [O II] is not excited in the broad-line region and only weakly excited in the

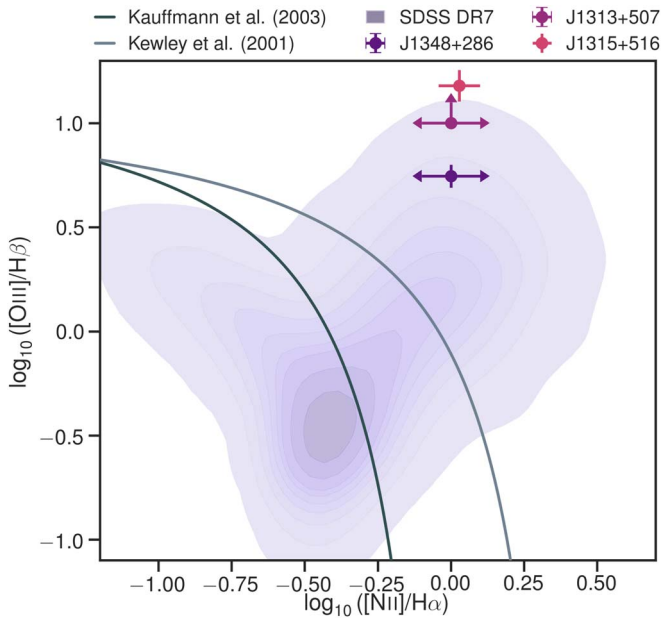


**Figure 3.** The Kauffmann et al. (2003) and Kewley et al. (2001) lines separate star-forming galaxies, composites, and AGN in the BPT diagram (Baldwin et al. 1981). The high [O III]/H $\beta$  narrow-line ratios securely classify J1348+286, J1313+507, and J1315+516 as Seyferts, even in the absence of [N II]/H $\alpha$  coverage. Given their high redshift of  $z > 1$ , none of the four required emission lines are covered for J1206+503 and J1154+513. The contours represent 10,000 sources sampled from SDSS DR7 (Abazajian et al. 2009).

narrow-line region (Vanden Berk et al. 2001). However, AGN can induce [O II] in extended emission line regions (EELRs) throughout the galaxy, which can bias high our SFRs (Maddox 2018).

We used the [O II] luminosity to SFR conversion from Kennicutt (1998):

$$\text{SFR} = (1.4 \pm 0.4) \times 10^{-41} L_{[\text{O II}]}, \quad (1)$$

where SFR is measured in  $M_{\odot} \text{ yr}^{-1}$  and  $L_{[\text{O II}]}$  is the total luminosity of the [O II] emission line in  $\text{erg s}^{-1}$ .

We compared the SFRs to values for typical star-forming galaxies (SFRs\*) at the same redshift using the parameterization from Sobral et al. (2014):

$$\text{SFR}^*(z) = 10^{0.55z+0.57}, \quad (2)$$

where SFR\* is measured in  $M_{\odot} \text{ yr}^{-1}$  and  $z$  is the redshift.

The SFRs of the sources and the typical SFRs at their redshift are listed in Table 4. Using [Ne V] to measure the EELR contribution in a stack of radio-loud quasars, Maddox (2018) found that  $\approx 50\%$  of the [O II] emission can be attributed to SF and  $\approx 50\%$  to EELRs. Three of our sources (J1315+516, J1154+513, J1206+503) have [O II]/[Ne V] ratios higher than the averages from Maddox (2018), ranging from 2.7 to 9, indicating a lower contamination from EELRs. On the other hand, our [O II] luminosities might be underestimated because no dust extinction correction was applied.

### 3.3. Mid-IR Color–Color Plots

We employ WISE W2 – W3 versus W1 – W2 color–color plots to separate AGN from galaxies, using the classification lines from Mingo et al. (2016). We used profile-fit photometry magnitudes without aperture corrections, given the high redshifts of our sources. J1348+286 could not be included in

**Table 4**  
[O II]-derived SFRs of the HyMoRS

Source	SFR ( $M_{\odot} \text{ yr}^{-1}$ )	SFR*( $z$ ) ( $M_{\odot} \text{ yr}^{-1}$ )
J1315+516	$5.1 \pm 1.5$	6.8
J1348+286	$33.8 \pm 10.9$	9.5
J1313+507	$14.0 \pm 4.2$	11.3
J1154+513	$115.8 \pm 34.2$	21.1
J1206+503	$31.9 \pm 9.9$	23.4

**Note.** No corrections for contamination from EELRs and dust absorption were applied. For comparison, we list the typical SFRs of star-forming galaxies at the redshift of each source.

this analysis because its proximity to another source impeded the proper deblending in the WISE data. The WISE color–color plot can be found in Figure 4.

## 4. Results and Discussion

### 4.1. Nature of the HyMoRS Host Galaxies

In this section, we combine insights from the color–color properties and the spectral analysis to obtain a consistent picture of the nature of our five sources. For detailed notes on each source, please see the Appendix.

The optical spectroscopy brings additional evidence to hone in on the AGN nature of the sources. Every source presents narrow lines and at least two broad ( $v_{\text{FWHM}} > 1000 \text{ km s}^{-1}$ ) emission lines, as shown in Table 3, securely identifying all sources as Type 1 AGN or quasars. Using the BPT diagram, we classify the narrow-line emission for the three lower redshift sources as dominated by the AGN narrow-line region instead of SF from H II regions (Figure 3). The Lorentzian, blueshifted, and/or winged [O III] profiles indicate significant turbulence and fast-moving clouds in the narrow-line regions and outflows. Moreover, all the sources have detections of [Ne V], which, with its very high 97 eV ionization potential, implies a hard ionizing spectrum decidedly associated with nuclear activity (Feltre et al. 2016). In our highest redshift source, the asymmetric CIV could be caused by nongravitational effects, such as dust scattering and radiation pressure as proposed by Baskin & Laor (2005). Among the five sources, J1348+286 has the strongest evidence for a quasar classification, given its power-law continuum. All four sources with WISE measurements are securely classified as AGN in the color–color diagnostic plot (see Figure 4). The sources occupy the same part of the color space ( $(W1 - W2) > 0.5$ ) as the bulk of HERGs and high-luminosity FR II sources (i.e., FR IIs located above the canonical  $L_{150 \text{ MHz}} \sim 10^{26} \text{ W Hz}^{-1}$  line; Mingo et al. 2022). By contrast, FR Is and lower luminosity FR IIs are almost exclusively located below the 0.5 line (Mingo et al. 2022). Our sources also fall within the AGN wedge of Mateos et al. (2012). Despite being clear AGN, our HyMoRS host galaxies display significant [O II] SFRs, typical of star-forming galaxies at their redshift. Therefore, even assuming 50% contamination of the [O II] fluxes by EELRs, our sources still have significant SFRs, which are comparable or higher than typical SFRs\* at their redshift ( $\text{SFR}/\text{SFR}^* \approx 0.4\text{--}2.7$ ).

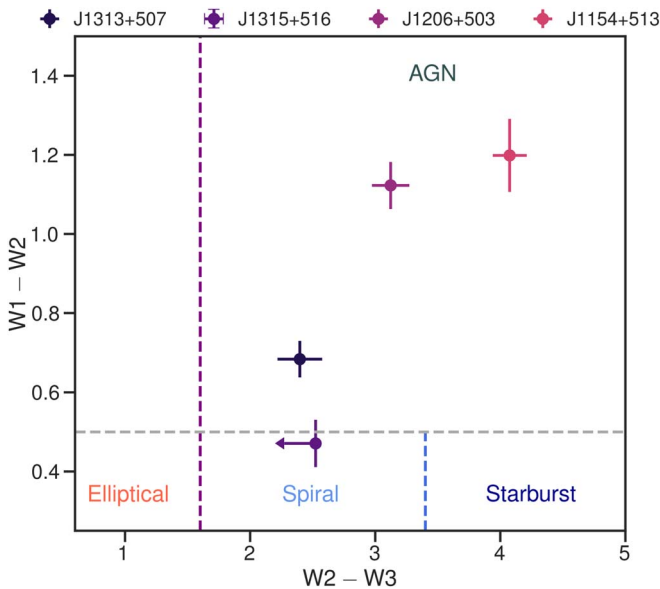


**Figure 4.** WISE W1–W2 vs. W2–W3 color-color plot, including the Mingo et al. (2016, 2022) lines that separate elliptical, spiral, and starburst galaxies, and active galactic nuclei (AGN). The four sources with secure WISE measurements are securely located in the AGN quadrant of this plot, where the bulk of FR IIs reside (Mingo et al. 2022).

#### 4.2. Are HyMoRS True FR I/II Hybrids?

Among the various HyMoRS formation models, we aim to determine whether the properties of the host galaxy could cause each of its radio jets to take on a different FR morphology. High-excitation emission lines are found almost exclusively in the spectra of high radio luminosity FR IIs (Mingo et al. 2022; Padovani et al. 2017). In line with our findings, these sources also have significant SFRs, indicative of ample gas supplies (Mingo et al. 2022). Given their SFRs ranging from 2.5 to  $58 M_{\odot} \text{ yr}^{-1}$ , our HyMoRS are hosted by typical star-forming galaxies. Supporting the FR II classification based on the high radio luminosities ( $L_{178 \text{ MHz}} \sim 10^{27} \text{ W Hz}^{-1} \text{ sr}^{-1}$ , which is well above the  $10^{25.5} \text{ W Hz}^{-1} \text{ sr}^{-1}$  FR I/FR II division line) and the spatially resolved spectral properties (Harwood et al. 2020), the optical and mid-IR data from the present paper paint a consistent picture: our HyMoRS are HERGs whose hosts are star-forming galaxies with strong Type 1 AGN/quasar features. Since radio quasars and Type 1 AGN are intrinsically radio galaxies with a narrower viewing angle (Padovani et al. 2017), our results thus indicate that, in a simplified scenario, HyMoRS might effectively be FR IIs in which the small angle between the radio jet and the line of sight of  $<45^{\circ}$  enables a clear view of both the narrow and broad-line regions. In reality, while the majority of Type 1 AGN are relatively unobscured, the torus covering factor can vary between individual AGN, resulting in a significant overlap between the covering factor distributions between Type 1 and Type 2 AGN (e.g., Elitzur 2012; Suh et al. 2019).

When originally discovered (Gawroński et al. 2006), and in subsequent large-scale survey searches (e.g., Kapińska et al. 2017; Mingo et al. 2019), HyMoRS candidates presented a compelling case for the existence of a hybrid FR I/II source. However, these initial searches did not benefit from wide-band, multifrequency data needed to disentangle their detailed morphology, especially if significant projection

effects are involved. Harwood et al. (2020) demonstrated that, in order to unequivocally classify the two sides as an FR I or FR II, detailed radio spectral analyses are required. Harwood et al. (2020) posited that the hybrid morphologies are actually caused by a combination of large-scale environmental effects pushing back FR II jets and a favorable orientation (see Figure 4 in Harwood et al. 2020). In another detailed multiwavelength study of a giant FR II radio galaxy that presents some HyMoRS-like asymmetry between the lobes, Seymour et al. (2020) conclude that the FR I-like jet is propagating into the dense intracluster medium (ICM) of the nearby irregular cluster, which slows it down. Such processes would compound with the ram pressure the ICM can exert on the radio jets, resulting in unusual morphologies that can be interpreted as hybrid sources when seen in projection. Our results seem to align with the conclusions from the detailed radio studies from Harwood et al. (2020) and Seymour et al. (2020). Unlike typical powerful FR IIs, which tend to be found, on average, in lower density environments than FR Is (e.g., Padovani et al. 2017; Mingo et al. 2019), the scenario that best fits the available data is that FR II HyMoRS would more likely be found in high-density environments, such as a low-mass cluster or group. The bent nature of the radio jets, as suggested by the scenario proposed by Harwood et al. (2020) implies significant relative motions between the HyMoRS and the large-scale environment responsible for the bending. Kapińska et al. (2017), for example, find that one of their sample of 25 HyMoRS is hosted by a cluster. Given the high SFRs, which indicate the presence of gas, the host galaxies could not have experienced much quenching as is typical for an overdense environment, such as a cluster. However, if HyMoRS are recent infallers into a cluster, that could explain both the relative motion and the star-forming nature of the host galaxy. To further test this hypothesis, we searched for evidence of overdensities within  $30'$  of the HyMoRS. The 10 ks Chandra exposure (PI: Kraft) targeting J1315+516 unveils a low surface brightness, extended area ( $\sim 5 \times 5 \text{ arcmin}^2$ ) toward the northeast of the source, with count density  $\sim 1.5$  times about the rest of the field. While this could indicate the presence of a group or cluster, a much deeper observation would be needed to conclusively determine whether an ICM is present. J1348+286 has accidental X-ray coverage with Chandra and XMM-Newton, but the low exposure times ( $<16$  ks) prevent a clear test of the overdensity hypothesis. Sunyaev–Zel’dovich detections in all-sky surveys, with, e.g., Planck, and optical search algorithms in all-sky photometric survey data have increasing errors and lower detection rates with redshift, high cluster mass limits ( $\sim 4 \times 10^{14} M_{\odot}$  at  $z > 0.5$ ; Planck Collaboration et al. 2016), as well as redshift upper limits for cluster detections (0.55 for redMaPPer; Rykoff et al. 2014), which prevent a clear conclusion regarding the presence of a cluster or group around our high redshift HyMoRS. The quality of the available data limits our ability to draw clear insights into the presence or absence of an overdensity around the HyMoRS, with deep, pointed observations being required.

## 5. Conclusions

In this work, we presented the first investigation into the nature of HyMoRS host galaxies with the goal of shedding light on the formation processes that drive the FR I/II dichotomy. Using primarily optical spectroscopy, we studied

the properties of the host galaxies of the five best-studied HyMoRS, which benefit from detailed radio investigations into their hybrid nature. We conclude that the HyMoRS in our sample are hosted by star-forming, disk galaxies with HERG spectral features typical of Type 1 AGN and quasars, which are almost exclusively found in powerful FR II sources. This sample of five was chosen as the most well-defined and best-studied HyMoRS examples. Though subsequent studies have identified more candidates using varied criteria, a larger follow-up study would be necessary to confirm that the conclusions here hold for the other HyMoRS population as a whole. Future deep, pointed, X-ray observations could further test the scenario that HyMoRS are infalling into a cluster that bends the jets because of the relative motion to the ICM. As proposed by Harwood et al. (2020), the hybrid morphology is likely caused by a favorable viewing angle, which makes one of the FR II jets appear to have an FR I configuration, as well as enabling a clear view of the narrow and broad-line region resulting in a Type 1 AGN/quasar optical classification. We thus predict that, unlike the broader FR II population, HyMoRS are likely to be found in galaxy cluster environments. However, deep, pointed X-ray observations are needed to fully test this hypothesis.

Gopal-Krishna & Wiita (2000) theorized that the existence of HyMoRS indicates that the black hole engine cannot alone determine the location of its jet hotspot; the morphological difference between the FR I and FR II classes. However, our results, albeit limited to a small sample of five, indicate that we have yet to find bona fide FR I/II hybrid sources. If all HyMoRS are bent FR II sources, this reopens the question about how the black hole engine influences the jets, further supporting findings from modern large-scale radio surveys (Mingo et al. 2022).

We thank the referee for the thoughtful comments that improved the paper. We also thank Matthew Ashby and Jonathan McDowell for stimulating discussions on potential avenues for the project. A.S. gratefully acknowledges the support of a Clay Fellowship. V.C. also acknowledges the Smithsonian Astrophysical Observatory REU program, which is funded in part by the National Science Foundation REU and Department of Defense ASSURE programs under NSF grant Nos. AST 1852268 and 2050813, and by the Smithsonian Institution. B.M. acknowledges support from the Science and Technology Facilities Council (STFC) under grant ST/T000295/1. We recognize and acknowledge the very significant cultural role and reverence that the summit of Maunakea has always had within the indigenous Hawaiian community. We are most fortunate to have the opportunity to conduct observations from this mountain. This publication makes use of data products from the Wide-field Infrared Survey Explorer, which is a joint project of the University of California, Los Angeles, and the Jet Propulsion Laboratory/California Institute of Technology, funded by the National Aeronautics and Space Administration.

*Facilities:* Gemini:Gillett, PS1, Sloan VLA, WISE.

*Software:* GLEAM (Stroe & Savu 2021), Astropy (Astropy Collaboration et al. 2013), APLpy (Robitaille & Bressert 2012), DS9 (Smithsonian Astrophysical Observatory 2000), Matplotlib (Barrett et al. 2005), SciPy (Virtanen et al. 2020).

## Appendix A Notes on Individual Sources

### A.1. J1315+516

Both the narrow and broad emission lines confirm this source as AGN-dominated. The narrow-line ratios firmly place the source in the Seyfert part of the BPT diagram (Figure 3). The AGN nature of the source is further supported by the broad Mg II and H $\alpha$  components, with velocity FWHM of over 5000 km s<sup>-1</sup> (Table 3). The source also has a significant detection of the very high ionization potential [Ne V] line. The source also has blueshifted outflows as indicated by the winged [O III]  $\lambda$ 5008.24 line. While the host galaxy is optically red, the galaxy has significant SF activity as traced by the [O II] emission, in line with typical star-forming galaxies at its redshift (see Sobral et al. 2014).

### A.2. J1348+286

J1348+286 is the brightest source in our sample, with emission line luminosities  $>10^{43}$  erg s<sup>-1</sup>. It has a point-like, quasar morphology in the optical imaging. The high S/N BOSS spectrum has a power-law continuum and strong Mg II and H $\beta$  line detections, which contain both broad (including Mg II  $v_{\text{FWHM}} > 11,000$  km s<sup>-1</sup>, H $\delta$  at over 3000 km s<sup>-1</sup>, and H $\gamma$  and H $\beta$  at over 5000 km s<sup>-1</sup>; Table 3) and narrow components, consistent with an orientation in which both the narrow and the broad-line regions are visible. Given its extreme [O III]/H $\beta$  ratio and the likely [N II]/H $\alpha$  ratio ranges, the source is securely placed in the Seyfert section of the BPT diagram (Figure 3). The [O III]  $\lambda$ 5008.24 emission has a Lorentzian shape with wings on either side, indicating blue- and redshifted outflows.

### A.3. J1313+507

A Type 2 source, J1313+507 has extremely broad, blueshifted Mg II emission, with  $v_{\text{FWHM}} > 20,000$  km s<sup>-1</sup> (Figure 1, Table 3). The presence of [Ne V] emission also confirms the AGN nature. The high  $S/N \sim 10$  [O III] detection and no H $\beta$  detection enable us to place a lower limit on the [O III]/H $\beta$  ratio indicating strong AGN contributions (Figure 3). The host galaxy SFR ( $13.9 \pm 4.2 M_{\odot} \text{ yr}^{-1}$ ) is consistent with typical star-forming galaxies at its redshift ( $11.3 M_{\odot} \text{ yr}^{-1}$ ; Sobral et al. 2014).

### A.4. J1154+513

J1206+503 is the highest redshift source in our sample and has the lowest S/N spectrum and faintest optical host ( $g > 22$  mag). Despite the low S/N, we detect broad Mg II and [Ne V], which confirms that the source is an AGN (Figure 1, Table 3). The [O II]-derived SFR of  $115.8 \pm 34.2 M_{\odot} \text{ yr}^{-1}$  is over five times higher than SFRs\*, classifying J1154+513 as a strongly star-forming source (Table 4).

### A.5. J1206+503

We detect C IV and Mg II with clearly broad profiles characteristic of AGN emission ( $>30,000$  and  $>14,000$  km s<sup>-1</sup>, respectively). C IV is asymmetric, with a blue excess, with Mg II containing a broad and narrow component.

## ORCID iDs

Andra Stroe  <https://orcid.org/0000-0001-8322-4162>  
 Victoria Catlett  <https://orcid.org/0000-0002-4925-8403>  
 Jeremy J. Harwood  <https://orcid.org/0000-0003-0251-6126>  
 Tessa Vernstrom  <https://orcid.org/0000-0001-7093-3875>  
 Beatriz Mingo  <https://orcid.org/0000-0001-5649-938X>

## References

- Abazajian, K. N., Adelman-McCarthy, J. K., Agüeros, M. A., et al. 2009, *ApJS*, **182**, 543
- Ahumada, R., Prieto, C. A., Almeida, A., et al. 2020, *ApJS*, **249**, 3
- Astropy Collaboration, Robitaille, T. P., Tollerud, E. J., et al. 2013, *A&A*, **558**, A33
- Baldwin, J. A., Phillips, M. M., & Terlevich, R. 1981, *PASP*, **93**, 5
- Barrett, P., Hunter, J., Miller, J. T., et al. 2005, in ASP Conf. Ser. 347, *Astronomical Data Analysis Software and Systems XIV*, ed. P. Shopbell et al. (San Francisco, CA: ASP), 91
- Baskin, A., & Laor, A. 2005, *MNRAS*, **356**, 1029
- Best, P. N., & Heckman, T. M. 2012, *MNRAS*, **421**, 1569
- Baum, S. A., & Heckman, T. 1989, *ApJ*, **336**, 681
- Bicknell, G. V. 1994, *ApJ*, **422**, 542
- Butler, A., Huynh, M., Delvecchio, I., et al. 2018, *A&A*, **620**, A16
- Celotti, A., Padovani, P., & Ghisellini, G. 1997, *MNRAS*, **286**, 415
- Dawson, K. S., Schlegel, D. J., Ahn, C. P., et al. 2013, *AJ*, **145**, 10
- Elitzur, M. 2012, *ApJL*, **747**, L33
- Fanaroff, B. L., & Riley, J. M. 1974, *MNRAS*, **167**, 31P
- Feltre, A., Charlot, S., & Gutkin, J. 2016, *MNRAS*, **456**, 3354
- Flewelling, H. A., Magnier, E. A., Chambers, K. C., et al. 2020, *ApJS*, **251**, 7
- Gawronski, M. P., Marecki, A., Kunert-Bajraszewska, M., et al. 2006, *A&A*, **447**, 63
- Gopal-Krishna, & Wiita, P. J. 1996, *ApJ*, **467**, 191
- Gopal-Krishna, & Wiita, P. J. 2000, *A&A*, **363**, 507
- Harwood, J. J., Vernstrom, T., & Stroe, A. 2020, *MNRAS*, **491**, 803
- Hickox, R. C., Jones, C., Forman, W. R., et al. 2009, *ApJ*, **696**, 891
- Janssen, R. M. J., Röttgering, H. J. A., Best, P. N., et al. 2012, *A&A*, **541**, A62
- Kaiser, C. R., & Alexander, P. 1997, *MNRAS*, **286**, 215
- Kaiser, C. R., & Best, P. N. 2007, *MNRAS*, **381**, 1548
- Kapińska, A. D., Terentev, I., Wong, O. I., et al. 2017, *AJ*, **154**, 253
- Kauffmann, G., Heckman, T. M., Tremonti, C., et al. 2003, *MNRAS*, **346**, 1055
- Kennicutt, R. C. 1998, *ARA&A*, **36**, 189
- Kewley, L. J., Dopita, M. A., Sutherland, R. S., et al. 2001, *ApJ*, **556**, 121
- Laing, R. A., Jenkins, C. R., Wall, J. V., et al. 1994, in ASP Conf. Ser. 54, *The First Stromlo Symp.: The Physics of Active Galaxies*, ed. G. V. Bicknell et al. (San Francisco, CA: ASP), 201
- Laing, R. A., & Bridle, A. H. 2002, *MNRAS*, **336**, 1161
- Maddox, N. 2018, *MNRAS*, **480**, 5203
- Mateos, S., Alonso-Herrero, A., Carrera, F. J., et al. 2012, *MNRAS*, **426**, 3271
- Mathews, T. A., Morgan, W. W., & Schmidt, M. 1964, *ApJ*, **140**, 35
- Mingo, B., Croston, J. H., Best, P. N., et al. 2022, *MNRAS*, **511**, 3250
- Mingo, B., Croston, J. H., Hardcastle, M. J., et al. 2019, *MNRAS*, **488**, 2701
- Mingo, B., Watson, M. G., Rosen, S. R., et al. 2016, *MNRAS*, **462**, 2631
- Miraghaei, H., & Best, P. N. 2017, *MNRAS*, **466**, 4346
- Ochsenbein, F., Bauer, P., & Marcout, J. 2000, *A&AS*, **143**, 23
- Padovani, P., Alexander, D. M., Assef, R. J., et al. 2017, *A&ARv*, **25**, 2
- Planck Collaboration, Ade, P. A. R., Aghanim, N., et al. 2016, *A&A*, **594**, A27
- Prestage, R. M., & Peacock, J. A. 1988, *MNRAS*, **230**, 131
- Robitaille, T., & Bressert, E. 2012, *APLpy: Astronomical Plotting Library in Python*, Astrophysics Source Code Library, ascl:1208.017
- Rykoff, E. S., Rozo, E., Busha, M. T., et al. 2014, *ApJ*, **785**, 104
- Salpeter, E. E. 1955, *ApJ*, **121**, 161
- Seymour, N., Huynh, M., Shabala, S. S., et al. 2020, *PASA*, **37**, e013
- Shaw, R. A. 2016, *GMOS Data Reduction Cookbook v1.2* (Tucson, AZ: National Optical Astronomy Observatory), <https://noirlab.edu/science/programs/csd/usngo/gmos-cookbook/>
- Smithsonian Astrophysical Observatory 2000, SAOImage DS9: A utility for displaying astronomical images in the X11 window environment, Astrophysics Source Code Library, ascl:0003.002
- Sobral, D., Best, P. N., Smail, I., et al. 2014, *MNRAS*, **437**, 3516
- Stroe, A., & Savu, V.-N. 2021, *GLEAM: Galaxy Line Emission and Absorption Modeling Astrophysics Source Code Library*, ascl:2102.030
- Suh, H., Civano, F., Hasinger, G., et al. 2019, *ApJ*, **872**, 168
- Vanden Berk, D. E., Richards, G. T., Bauer, A., et al. 2001, *AJ*, **122**, 549
- van Dokkum, P. G. 2001, *PASP*, **113**, 1420
- Virtanen, P., Gommers, R., Oliphant, T. E., et al. 2020, *NatMe*, **17**, 261
- White, R. L., Becker, R. H., Helfand, D. J., et al. 1997, *ApJ*, **475**, 479
- Wright, E. L., Eisenhardt, P. R. M., Mainzer, A. K., et al. 2010, *AJ*, **140**, 1868
- Wright, E. L., Eisenhardt, P. R. M., Mainzer, A. K., et al. 2019, *AllWISE Source Catalog (IPAC)*, [https://wise2.ipac.caltech.edu/docs/release/allwise/expsup/sec1\\_3.html#src\\_cat](https://wise2.ipac.caltech.edu/docs/release/allwise/expsup/sec1_3.html#src_cat)
- Zirbel, E. L., & Baum, S. A. 1995, *ApJ*, **448**, 521